PHYSICAL REVIEW E **108**, 044118 (2023)

Coarse-graining the vertex model and its response to shear

Gloria Triguero-Platero [*] and Falko Ziebert
Institute for Theoretical Physics, Heidelberg University, D-69120 Heidelberg, Germany

Luis L. Bonilla [†]
Department of Mathematics, Universidad Carlos III de Madrid, 28911 Leganés, Spain and G. Millán Institute for Fluid Dynamics, Nanoscience and Industrial Mathematics, Universidad Carlos III de Madrid, 28911 Leganés, Spain

(Received 8 February 2023; accepted 21 September 2023; published 9 October 2023)

Tissue dynamics and collective cell motion are crucial biological processes. Their biological machinery is mostly known, and simulation models such as the active vertex model exist and yield reasonable agreement with experimental observations such as tissue fluidization or fingering. However, a good and well-founded continuum description for tissues remains to be developed. In this work, we derive a macroscopic description for a two-dimensional cell monolayer by coarse-graining the vertex model through the Poisson bracket approach. We obtain equations for cell density, velocity, and the cellular shape tensor. We then study the homogeneous steady states, their stability (which coincides with thermodynamic stability), and especially their behavior under an externally applied shear. Our results contribute to elucidate the interplay between flow and cellular shape. The obtained macroscopic equations present a good starting point for adding cell motion, morphogenetic, and other biologically relevant processes.

DOI: 10.1103/PhysRevE.108.044118

I. INTRODUCTION

From the physical point of view, a tissue is a very complex material, since its constituents are active objects consuming energy and exerting forces onto the outside and between each other [1–5]. Individual cells are assembled into tissues by coupling to their neighbors through specific transmembrane protein complexes (cadherins), which build cell junctions. The latter physically link the actomyosin cortices of neighboring cells, enabling force transmission between them [1]. Many individual cellular processes (changes of cell shapes, cellular divisions, rearrangements, and extrusions) cause large-scale deformations of tissues. In the last few decades, extensive research has been devoted to understanding the links between cellular processes, tissue deformations, and cohesive coordinated cellular motion [5–10] responsible for wound healing assays [2,4,11], cancer progression [12–17], and morphogenesis [1,18–20]. A good macroscopic description of the mechanics and dynamics of tissue remains a major challenge at the interface of physics and biology, although there have been many proposals; see Refs. [5,21–25].

The main objective of this work is to derive a macroscopic description for a two-dimensional flat tissue such as an epithelial monolayer by a well-defined coarse-graining procedure. Successful and currently often-used mesoscopic models describing tissues as a network of cells that fill space with no gaps between cells exist: these are vertex and Voronoi models [18,26–29], first used to describe the physics of foams [30,31]. Interestingly, such models predict a jamming-unjamming (solid-liquid) transition at a critical mean shape index, which is the ratio between the mean cell perimeter and the square root of the mean cell area [32,33], and this has been observed in experiments [34]. Here, we use the Poisson bracket method [35,36] to coarse-grain the dynamics governed by the free energy of the vertex model. We obtain macroscopic—hydrodynamic—equations, which keep track of the underlying cellular structure due to the coupling to an equation for the average cellular shape tensor. We study the stability of the homogeneous phases, reflecting the above-mentioned transition, as well as the effects of externally shearing the layer at low rates. The response to high shear rates, as studied by simulations in Ref. [37], is outside the scope of the present paper. Note that, although the solid-liquid transition is present in the model derived here, we do not consider solid dynamics, as was done in Ref. [38].

In Sec. II, we briefly discuss the widely used active vertex model (AVM) [39]. It describes tissues as a network of polygonal cells forming a Voronoi tiling of the plane. In turn, the dual Delaunay triangulation of the plane uses the centers of the cells, which underlie a dynamics governed by the vertex free-energy function, as well as possibly additional active terms, typically intended to model cell motion. Note that in the following, we treat only the passive version. Usually overdamped dynamics is used in simulations [39], but underdamped dynamics with collective inertia has been recently proposed, allowing to capture more qualitative features of confluent cellular motion [17] seen in experiments [40,41].

The coarse-graining procedure is then briefly described in Sec. III, following largely Ref. [25]. At this point, the

---

[*] Present address: Bionanomechanics Lab, Institute of Micro and Nanotechnology, CSIC, 28760 Tres Cantos, Spain.

[†] Corresponding author: bonilla@ing.uc3m.es

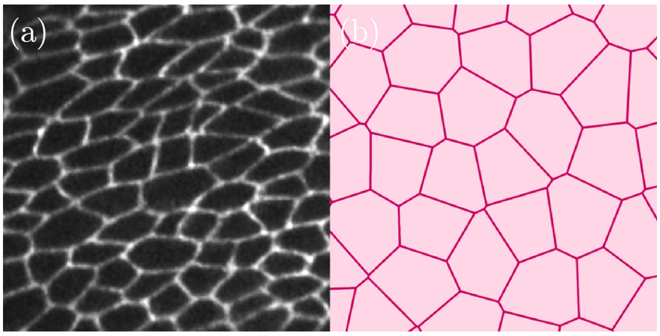

FIG. 1. (a) Apical view of the wing imaginal disk epithelium in the *Drosophila* embryo (modified from [43]). (b) Snapshot of a two-dimensional cell monolayer modeled by the AVM, implemented using the SAMoS software [44].

hydrodynamic equations are given with the dissipative part to be determined self-consistently, which is one of the main points of this work. In Sec. IV, we discuss the single-cell free-energy function of the homogeneous phases in terms of the shape tensor that is then decomposed in trace, anisotropy, and nematic-order-like tensor fields. We also discuss differences from previous works [25]. The thermodynamic stability of these homogeneous phases is then analyzed in Sec. V. These results are not new—they recover the stability of the ground state of the vertex model [42] and for an isotropic tissue [23] as obtained previously—but they are needed as a reference for the closed dynamical equations obtained later. In addition, we show that the solid-liquid transition at the critical shape index can be seen as a pitchfork bifurcation from isotropic to anisotropic phases at a critical value of the line tension. In Sec. VI we explain our choice of the Onsager dissipative coefficients, and we derive the resulting final continuum equations. The choice is motivated by the fact that the homogeneous steady states of the dynamic equations should be equivalent to the minima of the single-cell free energy. The dynamic stability of the homogeneous phases is then studied in Sec. VII. Finally, in Sec. VIII we investigate the stability under shear flow. We find an imperfect pitchfork bifurcation that highlights the usefulness of our dynamic equations. Section IX contains our conclusions.

II. ACTIVE VERTEX MODEL

Active vertex models (AVMs) are currently widely used to describe and infer data from epithelial tissues, representing them as two-dimensional (2D) networks of polygonal cells. The left panel in Fig. 1 shows an image of a *Drosophila* wing, in which the cell junctions have been visualized by fluorescent labeling. This picture clearly motivates such a modeling approach, as sketched on the right panel.

The properties and interactions of the cells constituting the monolayer are implemented in the AVM by defining a free-energy function that typically reads

$$\mathcal{F}=\sum_{\alpha=1}^{N}\left[\frac{\kappa_\alpha}{2}\left(A_\alpha-A_0^\alpha\right)^2+\frac{\Gamma_\alpha}{2}P_\alpha^2\right]+\sum_{\langle\mu\nu\rangle}\Lambda_{\mu\nu}l_{\mu\nu}. \qquad (1)$$

Here each cell is labeled by $\alpha=1,\dots,N$, and each vertex pair that shares a junction is designated by μ,ν. The first term implements an area elasticity, with κ_α the modulus of cell area A_α around A_0^α, its reference value. The second term is the perimeter contribution, with Γ_α the resistance of the cell to changing its perimeter P_α. Finally, $\Lambda_{\mu\nu}=\gamma_c-\frac{\omega}{2}$ is the line tension of the cell junctions of length $l_{\mu\nu}$ that results from the cortical tension γ_c along the contacts between cells and the cell-cell adhesion energy ω. The implementation of the vertex model dynamics then rearranges the positions of all vertices, trying to minimize the energy function for a given set of parameters.

While the moduli κ_α and Γ_α are positive, $\Lambda_{\mu\nu}<0$. When the cell α shares junctions only with other cells of the same type, $\sum_{\langle\mu,\nu\rangle}\Lambda_{\mu\nu}l_{\mu\nu}=\Lambda_{\mu\nu}\sum_{\langle\mu,\nu\rangle}l_{\mu\nu}=\Lambda_{\mu\nu}P_\alpha$, and this term can be put together with the perimeter term, thereby yielding $\frac{\Gamma_\alpha}{2}(P_\alpha-P_0^\alpha)^2$ plus an unimportant constant, provided the target perimeter is $P_0^\alpha=-\Lambda_{\mu\nu}/\Gamma_\alpha>0$. The *shape index* [33],

$$p_0^\alpha=\frac{P_0^\alpha}{\sqrt{A_0^\alpha}}=\frac{|\Lambda_{\alpha\beta}|}{\Gamma_\alpha\sqrt{A_0^\alpha}}, \qquad (2)$$

characterizes the ratio of the cell perimeter to the square root of its area. A critical value of this quantity is $p^{0*}=3.812$, which separates fluidlike and solidlike behavior of the tissue [33,45]: for $p^0<p^{0*}$, the monolayer is solidlike, and for $p^0>p^{0*}$, it displays fluidlike behavior. Solidlike cells tend to be close to regular polygons and rarely give rise to fingering instabilities, whereas for fluidlike cells one finds both fingering instabilities and irregular cell shapes.

In the standard implementation of the AVM, the cells in the monolayer satisfy the following overdamped equations of motion [39]:

$$\zeta\dot{\boldsymbol{r}}_\alpha=f_a\boldsymbol{n}_\alpha+\boldsymbol{F}_\alpha+\nu_\alpha \qquad (3)$$

and

$$\zeta^r\dot{\theta}_\alpha=\boldsymbol{\tau}_\alpha\cdot\boldsymbol{N}_\alpha+\nu_\alpha^r. \qquad (4)$$

The unknowns $\boldsymbol{r}_\alpha$ and θ_α are the positions of the centers of mass and the orientations of the directors of each cell α, defined as $\boldsymbol{n}_\alpha=(\cos\theta_\alpha,\sin\theta_\alpha)$. In the center-of-mass equation, $f_a\boldsymbol{n}_\alpha$ are active self-propulsion forces along the vector $\boldsymbol{n}_\alpha$ determining the direction of cell motion, $\boldsymbol{F}_\alpha$ are gradient forces arising from the free-energy function, Eq. (1), ν_α are stochastic forces, and ζ is a friction coefficient. In the angular equation, $\boldsymbol{\tau}_\alpha$ and $\boldsymbol{N}_\alpha$ are the torque, stemming from cell-cell alignment models and acting on the vector $\boldsymbol{n}_\alpha$, and the normal vector to the cell monolayer (unit vector along the z-axis). ν_α^r is a rotational noise and ζ^r is the rotational friction. Both noise terms are usually implemented as Gaussian white noise.

In the following, we use a coarse-graining procedure that is Hamiltonian in nature. Hence we do not use Eqs. (3) and (4), but rather we study a fluid of deformable particles, without active contributions. Nevertheless, the Poisson bracket approach accounts for the dissipative contributions in the hydrodynamic limit, and we will treat the vertex free-energy function, Eq. (1), as faithfully as possible to keep track of the cellular nature of the system, especially the sensitivity to the shape index/line tension.

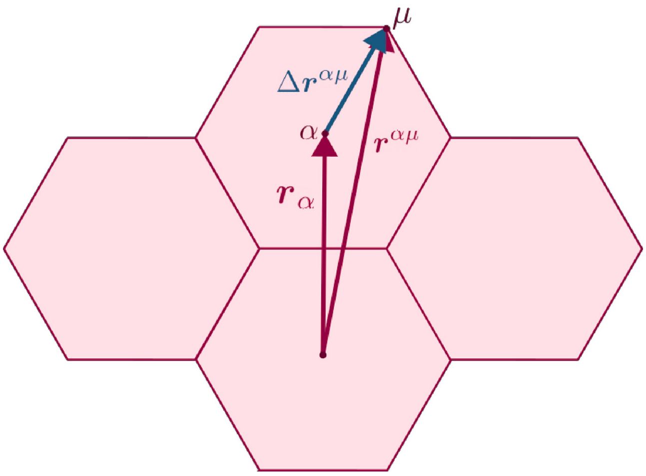

FIG. 2. Definition of the vectors that are used to build up the shape tensor. The position of the cell center α is given by $\boldsymbol{r}_\alpha$, and that of vertex μ of cell α is $\boldsymbol{r}^{\alpha\mu}$. Then, $\Delta\boldsymbol{r}^{\alpha\mu} = \boldsymbol{r}^{\alpha\mu} - \boldsymbol{r}_\alpha$.

III. COARSE-GRAINING PROCEDURE USING POISSON BRACKETS

Our objective is to derive hydrodynamic equations for a fluid formed by deformable polygonal-shaped particles that is governed by the free energy of the AVM, Eq. (1). Unlike the AVM, we shall not include active forces in our equations. Thus, the equations will only reflect the effects of the fluid flow on cell shape and vice versa.

On large scales, this fluid is described by the average (coarse-grained) hydrodynamic fields ϕ^a, which are the mass density ρ, the momentum density $\boldsymbol{g}$, and the cell-shape density tensor G. The latter accounts for the shape and elongation of the cells. The "microscopic" versions of the hydrodynamic fields are [25]

$$\hat\rho(\boldsymbol{r}, t) = \sum_{\alpha\mu} m^\alpha \delta(\boldsymbol{r} - \boldsymbol{r}^{\alpha\mu}(t)), \tag{5}$$

$$\hat{\boldsymbol{g}}(\boldsymbol{r}, t) = \sum_{\alpha\mu} \boldsymbol{g}_\alpha \delta(\boldsymbol{r} - \boldsymbol{r}^{\alpha\mu}(t)), \tag{6}$$

$$\hat G^\alpha_{ij}(\boldsymbol{r}, t) = \sum_{\alpha} G^\alpha_{ij} \delta(\boldsymbol{r} - \boldsymbol{r}^{\alpha}(t)), \tag{7}$$

$$G^\alpha_{ij} = \frac{1}{n}\sum_{\mu=1}^{n} \Delta x_i^{\alpha\mu} \Delta x_j^{\alpha\mu}. \tag{8}$$

Here m^α is the mass of cell α (we use $m^\alpha = 1$), and $\boldsymbol{r}^{\alpha\mu}$ is the position of vertex μ. The momentum of cell α is given by $\mathbf{g}_\alpha = m^\alpha \dot{\mathbf{r}}_\alpha$ and the shape tensor as specified via the vertices, with $\Delta x_i^{\alpha\mu} = \mathbf{r}^{\alpha\mu} - \mathbf{r}_\alpha$, where $\mathbf{r}_\alpha = \sum_\mu \mathbf{r}^{\alpha\mu}/n$ is the center of mass of the cell, and Latin indices denote components; see Fig. 2. Note that the mass and momentum density fields are defined through the positions of the vertices in the δ function, while the shape tensor uses δ functions centered at the cell centers. This is due to the definition of the shape tensor in Eq. (8), which already includes all vertices from each cell and is defined only for each cell center.

To obtain continuum equations for the hydrodynamic fields ϕ^α from the vertex model, we could resort to the Mori-Zwanzig projection technique [46]. However, although thought for different microscopic dynamics, it is easier to use the Poisson bracket approach, which is known to produce the usual hydrodynamics for nondeformable (and possibly anisotropic) particles [35,36,47]. Given microscopic Hamiltonian dynamics, the evolution of a microscopic function $\hat\phi(\mathbf{r}, t)$ obeys the equation

$$\frac{\partial\hat\phi}{\partial t} = \{\hat{\mathcal{H}}, \hat\phi\} = \sum_\alpha \frac{\partial\hat{\mathcal{H}}}{\partial g_j^\alpha}\frac{\partial\hat\phi}{\partial r_j^\alpha} - \frac{\partial\hat\phi}{\partial g_j^\alpha}\frac{\partial\hat{\mathcal{H}}}{\partial r_j^\alpha}, \tag{9}$$

where the Hamiltonian function $\hat{\mathcal{H}}$ depends on the cellular positions and momenta $\mathbf{r}^\alpha$ and $\mathbf{g}^\alpha$. The coarse-graining operation consists of a spatial average on a length scale comprising many cells that is still small compared to macroscopic lengths. Given a coarse-grained free energy, $\mathcal{F}$, which depends on the macroscopic fields $\phi^a = \rho, \mathbf{g}, G$, the coarse-grained equations are [25,36]

$$\frac{\partial\phi^a}{\partial t} = \{\mathcal{F}, \phi^a\} - \Gamma^{ab}\frac{\delta\mathcal{F}}{\delta\phi^b}, \tag{10}$$

$$\{\mathcal{F}, \phi^a\} = -\int d^2x' \mathcal{P}_{ab}(\boldsymbol{r}, \boldsymbol{r}')\frac{\delta\mathcal{F}}{\delta\phi^b(\boldsymbol{r}')}, \tag{11}$$

$$\mathcal{P}_{ab}(\boldsymbol{r}, \boldsymbol{r}') = \{\phi^a(\boldsymbol{r}), \phi^b(\boldsymbol{r}')\} = -\mathcal{P}_{ba}(\boldsymbol{r}', \boldsymbol{r}), \tag{12}$$

where summing over repeated indices is intended, and we have dropped the time variable for now. The term $\{\mathcal{F}, \phi^a\}$ in Eq. (10) yields the reactive part of the evolution equations, and the other term yields the dissipative part. The latter is proportional to the generalized forces, as defined by variations of the free energy, times kinetic coefficients Γ^{ab} that obey Onsager reciprocity relations near equilibrium [48]. The coarse-grained Poisson brackets $\{\phi^a, \phi^b\}$, especially for the shape tensor, have been calculated previously in Ref. [25].

The free energy can be split in a kinetic and a potential part

$$\mathcal{F}(\phi^a) = \int d^2x(f_K + f_V), \tag{13}$$

$$f_K = \sum_{i=1}^{2}\frac{g_i^2}{2\rho} = \sum_{i=1}^{2}\frac{1}{2}\rho v_i^2, \quad f_V = f_{\rm sc} + f_{\rm int}. \tag{14}$$

The kinetic free energy is the usual one in terms of the average velocity $\mathbf{v} = \mathbf{g}/\rho$. The potential free energy is split into an average containing only single-cell quantities, $f_{\rm sc}$, and an interaction with neighboring cells, which, in analogy to nematic liquid crystals [49], is assumed to be

$$f_{\rm int} = \frac{K_G}{2}\left(\frac{\partial G_{kl}}{\partial x_i}\right)^2. \tag{15}$$

This assumption is motivated by the fact that tissues share many properties of (active) nematic liquid crystals concerning their anisotropy and defect structure [50]. Note that it could be necessary to introduce more elastic constants. However, in so far as dedicated experimental measurements of these constants remain an open task, we keep the simple form (15). For a homogeneous phase with constant hydrodynamic fields, $f_K = f_{\rm int} = 0$, and the free-energy density is $f = f_{\rm sc}$. In the next section, we will find an expression for $f_{\rm sc}$ from Eq. (1) in terms of the trace and deviatoric parts of the shape tensor.

With the splitting of Eq. (13), the equations of motion (10) become

$$\frac{\partial \rho}{\partial t} + \nabla \cdot (\rho \boldsymbol{v}) = 0, \tag{16}$$

$$\rho \frac{d}{dt} v_i = -\partial_i p + \partial_j \left(\sigma^D_{ij} + \sigma^E_{ij} + \sigma^G_{ij} \right), \tag{17}$$

$$\frac{D}{Dt} G_{ij} = G_{ik} D_{kj} + D_{ik} G_{kj} - \Gamma_{ijkl} \frac{\delta \mathcal{F}}{\delta G_{kl}}. \tag{18}$$

These equations have already been deduced in [25]. There, the authors introduced an additional dynamic anisotropy density field $M(\mathbf{r}, t)$ by splitting off a contribution from the shape tensor already at the level of the Poisson brackets. We deemed this unnecessary, since by treating the free energy of the vertex model faithfully, see Sec. IV below, all the information about anisotropy should be properly accounted for. Here $\partial_i = \partial/\partial x_i$, and

$$\partial_i v_j = D_{ij} + \omega_{ij} + \frac{1}{2} \delta_{ij} \nabla \cdot \boldsymbol{v}, \tag{19}$$

$$D_{ij} = \frac{1}{2} (\partial_i v_j + \partial_j v_i - \delta_{ij} \nabla \cdot \boldsymbol{v}), \tag{20}$$

$$\omega_{ij} = \frac{1}{2} (\partial_i v_j - \partial_j v_i), \tag{21}$$

$$\frac{d}{dt} = \frac{\partial}{\partial t} + \mathbf{v} \cdot \nabla, \quad \frac{D}{Dt} = \frac{d}{dt} - [\omega, \cdot] \tag{22}$$

are the gradient of the average velocity, the deviatoric part of its symmetrization (the rate of strain tensor), the vorticity, the material derivative, and the corotational derivative, respectively. In the latter, $[A, B]_{ij} = A_{ik} B_{kj} - B_{ik} A_{kj}$. The continuity equation (16) does not contain a dissipative part. The pressure, and the different stress tensor contributions entering Eq. (17), are [25]

$$p = \rho \frac{\delta \mathcal{F}_V}{\delta \rho} - f, \tag{23}$$

$$\sigma^D_{ij} = 2\eta D_{ij} + \eta_b \delta_{ij} \nabla \cdot \mathbf{v}, \tag{24}$$

$$\sigma^E_{ij} = -\frac{\partial f_{\text{int}}}{\partial(\partial_j G_{kl})} \partial_i G_{kl} = -K_G \partial_i G_{kl} \partial_j G_{kl}, \tag{25}$$

$$\sigma^G_{ij} = 2 G_{jk} \frac{\delta \mathcal{F}_V}{\delta G_{ik}} - \delta_{ij} G_{kl} \frac{\delta \mathcal{F}_V}{\delta G_{kl}}. \tag{26}$$

For the sake of simplicity, in Eq. (24) we assumed that the dissipative part of the stress tensor, σ^D_{ij}, is that of an isotropic fluid with shear and bulk viscosity coefficients η and η_b, respectively. In uniaxial anisotropic situations, one expects five instead of just these two viscosities [49]. The contributions σ^E_{ij} and σ^G_{ij} are reactive, and the former corresponds to Ericksen stresses in liquid crystals [49]. The coefficient tensor Γ_{ijkl} in Eq. (18) will be derived later, after we have analyzed the free energy of the homogeneous phases.

It should be noted that Eqs. (16)–(18) are clearly of a hydrodynamic nature, i.e., they describe a, possibly anisotropic, tissue at timescales where flow is important. They cannot account for any elastic response beyond what is implemented in the vertex free-energy function (area elasticity and liquid-crystal-like anisotropic elasticity).

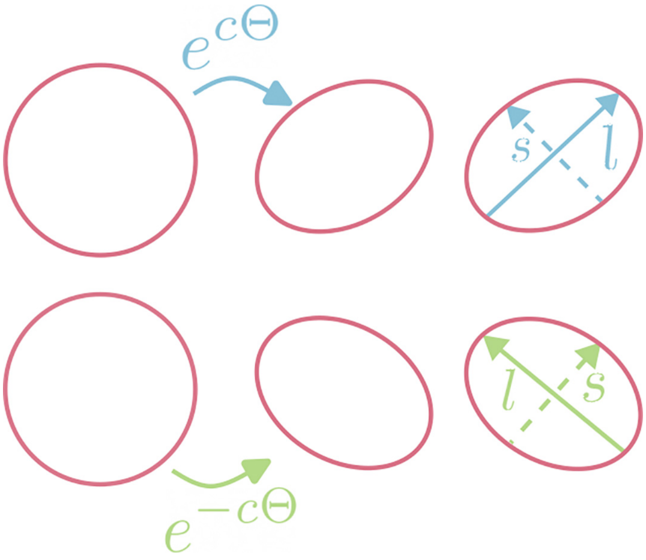

FIG. 3. Sketch of the anisotropic states of a cell with $c > 0$ (upper row) vs $c < 0$ (lower row). For a given orientation angle θ, $c > 0$ aligns the long axis of the ellipse, l, and the θ direction, whereas $c < 0$ aligns the short axis of the ellipse, s, and the θ direction.

IV. HOMOGENEOUS FREE-ENERGY DENSITY OF THE VERTEX MODEL

Let us assume that the cells are regular (or almost regular) n-sided polygons. We also assume that κ, A_0, Γ, and Λ are the same for all the cells, and we use $\sum_{\langle \mu\nu \rangle} l_{\mu\nu} = P$ (perimeter). Then the cellular area and perimeter are given in terms of the shape tensor G by [25]

$$A_\alpha = \mu \sqrt{\det(G)}, \quad P_\alpha = \nu \sqrt{\text{Tr}(G)}, \tag{27}$$

$$\mu = \frac{n}{2} \sin\left(\frac{2\pi}{n}\right), \quad \nu = n\sqrt{2} \sin\left(\frac{\pi}{n}\right), \tag{28}$$

with $n = 6$ for hexagons. For such a homogeneous phase with a single type of cells, Eq. (1) results in the following expression for the vertex free-energy density:

$$f_{\text{sc}} = \frac{\kappa}{2} [\mu \sqrt{\det(G)} - A_0]^2 + \frac{\Gamma \nu^2}{2} \text{Tr}(G) + \Lambda \nu \sqrt{\text{Tr}(G)}, \tag{29}$$

where the cell area has been absorbed in the positive constants κ, Γ, and in $\Lambda < 0$. Note that Eq. (29) reflects only single-cell properties.

Following Ref. [23], we write the shape tensor as

$$G = M_0 e^{c\Theta} = M_0 (\cosh c\, I + \sinh c\, \Theta), \tag{30}$$

where M_0 and c are scalar fields, I is the identity, and Θ is the traceless symmetric tensor field

$$\Theta = \begin{pmatrix} \cos 2\theta & \sin 2\theta \\ \sin 2\theta & -\cos 2\theta \end{pmatrix}. \tag{31}$$

Note that $M_0^2 = \det(G)$ and $\Theta^2 = I$ hold. Importantly, $c = 0$ yields an isotropic shape tensor with $\text{Tr}(G) = 2\sqrt{\det(G)}$. Thus, c measures the anisotropy of the cells. The angle θ in Eq. (31) determines the direction of the eigenvector corresponding to the largest eigenvalue of G. Figure 3 sketches the anisotropic states of an elliptic cell with nonzero c. A related decomposition has been used directly on a triangular tiling of the plane representing a cellular tissue in Ref. [24]. However, Eq. (30) is easier to relate to the free energy of Eq. (29) written in terms of the average shape tensor.

In terms of $R = \mathrm{Tr}(G)$, we can rewrite Eq. (30) as

$$G = \frac{R}{2}(I + \tanh c\,\Theta), \qquad \tilde{G} = \frac{R}{2}\tanh c\,\Theta, \tag{32}$$

where the traceless tensor $\tilde{G}$ is the deviatoric part of the shape tensor. Note its similarity to the order parameter of nematic liquid crystals [49]. Thus, we can rewrite the vertex free energy density Eq. (29) in the following simple form:

$$f_{\mathrm{sc}} = \frac{\kappa}{2}\left(\frac{\mu R}{2\cosh c} - A_0\right)^2 + \frac{\Gamma\nu^2 R}{2} + \Lambda\nu\sqrt{R}\,. \tag{33}$$

Looking at Eq. (32), the fields R, $R\tanh c$, and θ occurring in the shape tensor parametrization describe the cell perimeter, the shape anisotropy, and the director angle, respectively. As R and c appear naturally in the shape tensor and enter the free-energy density, Eq. (33), there is no need to introduce a specific anisotropy field or to postulate a connection of the latter to the orientational order, as had been done previously in Ref. [25].

V. THERMODYNAMIC STABILITY

The minima of the vertex free energy, Eq. (33), correspond to stable homogeneous phases. At them, the first derivatives of f_{sc} vanish, which yields the conditions

$$\frac{\partial f_{\mathrm{sc}}}{\partial R} = \frac{\kappa\mu}{2\cosh c}\left(\frac{\mu R}{2\cosh c} - A_0\right) + \frac{\nu}{2}\left(\Gamma\nu + \frac{\Lambda}{\sqrt{R}}\right) = 0\,, \tag{34a}$$

$$\frac{\partial f_{\mathrm{sc}}}{\partial c} = -\frac{\kappa\mu R\sinh c}{2\cosh^2 c}\left(\frac{\mu R}{2\cosh c} - A_0\right) = 0\,. \tag{34b}$$

Figure 4 shows graphically that solutions to Eq. (34a) exist only if the line tension is nonpositive or, in the case of anisotropic phases, negative. In turn, Eq. (34b) has isotropic solutions $c = 0$ and $\pm c$-symmetric anisotropic solutions only for $R > 2A_0/\mu$, as is evident from the bracket term and also shown graphically in Fig. 5. Anisotropic solutions have $A = A_0$, and hence from Eq. (34a) it can be deduced that $\sqrt{R} = |\Lambda|/(\Gamma\nu)$, i.e., $P = |\Lambda|/\Gamma$. These phases are stable if and only if the Hessian matrix of f_{sc} is positive-definite, which is equivalent to

$$\frac{\partial^2 f_{\mathrm{sc}}}{\partial R^2} = \frac{\kappa\mu^2}{4\cosh^2 c} - \frac{\nu\Lambda}{4R^{\frac{3}{2}}} > 0\,, \tag{35a}$$

$$\frac{\partial^2 f_{\mathrm{sc}}}{\partial c^2} = \frac{\kappa\mu R}{4\cosh^2 c}[2A_0\cosh c(1 - 2\tanh^2 c) - \mu R(1 - 3\tanh^2 c)] > 0\,, \tag{35b}$$

$$\frac{\partial^2 f_{\mathrm{sc}}}{\partial R^2}\frac{\partial^2 f_{\mathrm{sc}}}{\partial c^2} - \left(\frac{\partial^2 f_{\mathrm{sc}}}{\partial R\partial c}\right)^2 > 0\,. \tag{35c}$$

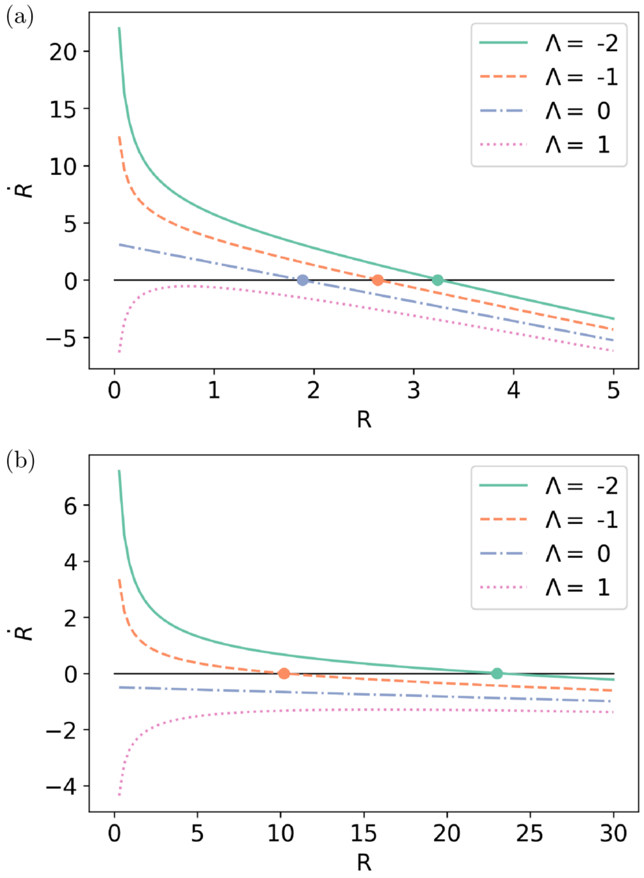

FIG. 4. Graphical solution of $\partial f_{\mathrm{sc}}/\partial R = 0$ by showing $\dot{R} = -\partial f_{\mathrm{sc}}/\partial R$ vs R for different values of the line tension Λ. The parameters are $\kappa = 1$, $n = 6$ (hexagons), $\Gamma = 0.1$, and $A_0 = \pi$. (a) Isotropic case, $c = 0$; (b) an anisotropic case with $c = 3$.

A. Cell shape instability and bifurcation

Let us assume that the cell perimeter is constant, and we want to ascertain whether phases with isotropic cells $(c = 0)$ are stable. If this is the case, $c = 0$ has to be a minimum of the free energy. Writing $\mathrm{sech}\, c = \sqrt{1 - \tanh^2 c} \simeq 1 - \frac{1}{2}\tanh^2 c$ in Eq. (33), we

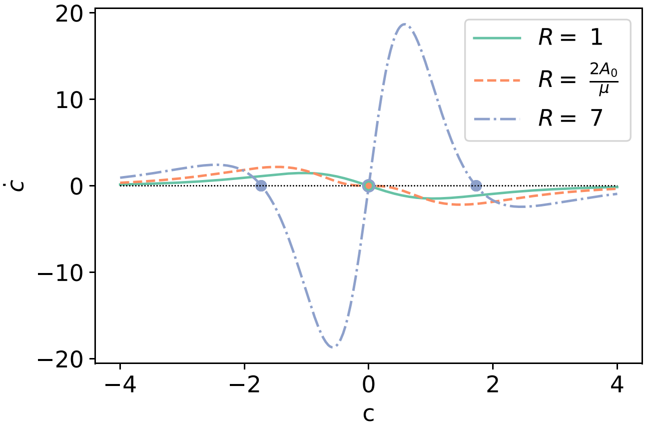

FIG. 5. Graphical solution of $\partial f_{\mathrm{sc}}/\partial c = 0$ by showing $\dot{c} = -\partial f_{\mathrm{sc}}/\partial c$ vs c for different values of R, proportional to the squared perimeter. Shown are the three cases $R < R^*$, $R = R^* = 2A_0/\mu$, and $R > R^*$. The parameters are $\kappa = 1$, $n = 6$ (hexagons), $\Gamma = 0.1$, and $A_0 = \pi$.

obtain

$$\begin{aligned} f_{\mathrm{sc}} - f_0 &\simeq \frac{\kappa\mu R A_0}{4}\left[\left(1-\frac{\mu R}{2A_0}\right)\tanh^2 c + \frac{1}{4}\tanh^4 c\right] \\ &\simeq \frac{\kappa\mu R A_0 c^2}{4}\left[1-\frac{\mu R}{2A_0}+\frac{1}{3}\left(\frac{\mu R}{A_0}-\frac{5}{4}\right)c^2\right] \end{aligned} \quad (36)$$

up to order $O(c^6)$ and where f_0 is constant. Using Eq. (27), for a fixed perimeter we get $R = P_0^2/\nu^2 = \Lambda^2/(\Gamma^2\nu^4)$, and we obtain

$$\begin{aligned} f_{\mathrm{sc}} = f_0 &+ \frac{\kappa\mu^2 P_0^2 A_0 c^2}{8\nu^4}\left[\frac{2\nu^2}{\mu}-\frac{P_0^2}{A_0}+\frac{1}{3}\left(\frac{2P_0^2}{A_0}-\frac{5\nu^2}{2\mu}\right)c^2\right] \\ &+ O(c^6). \end{aligned} \quad (37)$$

Clearly, the isotropic solution $c = 0$ is stable when the shape index p_0 as defined in Eq. (2) is smaller than a critical value given by

$$p_0^* = \frac{P_0}{\sqrt{A_0}} = \sqrt{\frac{2\nu^2}{\mu}} = \sqrt{4n\tan\left(\frac{\pi}{n}\right)}, \quad (38)$$

where we used Eq. (28). At $p_0 = p_0^*$, the single-cell free-energy density deviates from that of the isotropic phase as $f_{\mathrm{sc}} - f_0 \simeq \kappa\nu^2 A_0^2 c^4/8 \geqslant 0$. For $p_0 < p_0^*$, the isotropic phase is stable, corresponding to a solidlike structure with cells being almost regular polygons; see Fig. 2 of [42] for critical lines on the plane (Λ, Γ) corresponding to $n = 3, 4, 5, 6$. For $p_0 > p_0^*$, a finite $c \neq 0$ emerges, corresponding to cells having irregular anisotropic shapes. It has been shown in [42] that the shear modulus for the hexagonal lattice is finite and vanishes at p_0^*: there is a rigidity transition separating solidlike phases, where cells have to put in some work in order to rearrange, and liquidlike phases (soft lattices [42]) with no energy cost for rearranging cells [33]. For a disordered cellular tissue, the rigidity transition was shown numerically to occur at $p_0^* \approx 3.81$ [33]. Interestingly, this corresponds to $n = 5$, although pentagons cannot tile the plane. If one considers a hexagonal tiling, $n = 6$, we obtain $p_0^* \approx 3.72$, as already given in [42]. Figure 6 shows the single-cell free-energy density, Eq. (33), as a function of c for different values of Λ, and it illustrates how the anisotropic phase appears.

Equation (37) is an approximation of Eq. (33), which, for a fixed perimeter $P_0 = |\Lambda|/\Gamma$ and $\Lambda < 0$, becomes

$$f_{\mathrm{sc}} = \frac{\kappa\mu^2\Lambda^4}{8\Gamma^4\nu^4}\left(\operatorname{sech} c - \frac{2A_0\Gamma^2\nu^2}{\mu\Lambda^2}\right)^2 - \frac{\Lambda^2}{2\Gamma}. \quad (39)$$

Similarly, fixing the area to A_0, $\sqrt{R} = \sqrt{2A_0\cosh c/\mu}$, and Eq. (33) becomes

$$f_{\mathrm{sc}} = \frac{\Gamma\nu^2 A_0}{\mu}\left(\sqrt{\cosh c} - \sqrt{\frac{\mu\Lambda^2}{2A_0\Gamma^2\nu^2}}\right)^2 - \frac{\Lambda^2}{2\Gamma}. \quad (40)$$

For $p^0 > p^{0*}$, the values of c that solve Eq. (34b) are either $c = 0$ or

$$\cosh c = \frac{\mu\Lambda^2}{2A_0\Gamma^2\nu^2}. \quad (41)$$

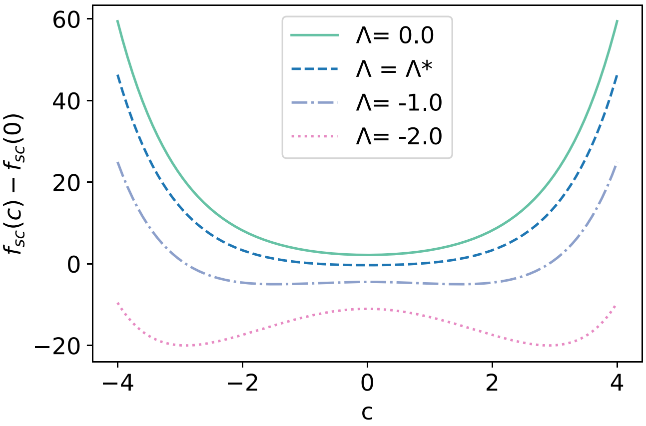

FIG. 6. Normalized homogeneous free-energy density vs anisotropy c for different values of Λ as indicated in the inset. The dashed line corresponds to the critical line tension given by Eq. (38) with $\Lambda^* = -P_0\Gamma = -\Gamma\sqrt{4A_0 n\tan(\pi/n)}$. Parameter values are $\kappa = 1$, $n = 6$, $\Gamma = 1.5$, and $A_0 = \pi$.

Solutions of this equation with $c \neq 0$ correspond to anisotropic phases, which are stable, as evident according to either Eqs. (39), (40), or the criteria (35), which simply become

$$\frac{\partial^2 f_{\mathrm{sc}}}{\partial R^2} = \frac{\kappa A_0^2}{R^2} + \frac{\Gamma\nu^2}{4R} > 0\,, \quad \frac{\partial^2 f_{\mathrm{sc}}}{\partial c^2} = \kappa A_0^2\tanh^2 c > 0,$$

$$\frac{\partial^2 f_{\mathrm{sc}}}{\partial R^2}\frac{\partial^2 f_{\mathrm{sc}}}{\partial c^2} - \left(\frac{\partial^2 f_{\mathrm{sc}}}{\partial R\partial c}\right)^2 = \frac{\kappa\Gamma\nu^2 A_0^2}{4R}\tanh^2 c > 0.$$

We can now draw the bifurcation diagram of anisotropy c versus the line tension Λ as the control parameter, with its critical value $\Lambda^* = -\Gamma\nu\sqrt{2A_0/\mu}$ obtained from Eq. (38). The bifurcation diagram, displaying a pitchfork bifurcation, is shown in Fig. 7. Cells with $c > 0$ and $c < 0$ have the same free energy (since there is no preferred direction in the free energy), but different orientations; cf. Fig. 3 [23,24].

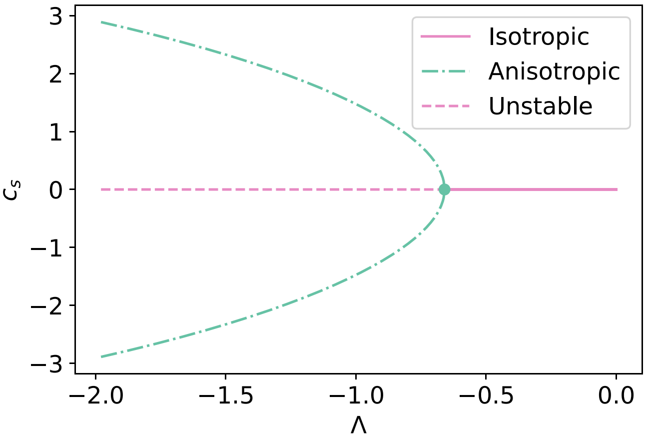

FIG. 7. Pitchfork bifurcation in the plane (Λ, c), occurring at a critical line tension value $\Lambda^* = -\Gamma\nu\sqrt{2A_0/\mu}$. For $\Lambda > \Lambda^*$, the isotropic solution, $c = 0$, is the only stationary state and stable. For $\Lambda < \Lambda^*$, the isotropic state becomes unstable (dashed line) and the system chooses one of the symmetric anisotropic branches.

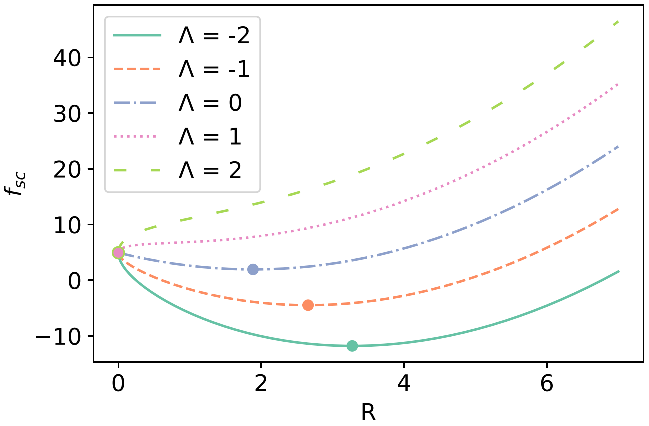

FIG. 8. Single-cell free-energy density of the isotropic homogeneous state ($c = 0$) as a function of R for different line tension values Λ, with $\kappa = 1$, $n = 6$ (hexagons), $\Gamma = 0.1$, and $A_0 = \pi$. The minimum of the free energy at $R^* > 0$ disappears for sufficiently large positive values of the line tension.

B. Cell area instability of the isotropic phase

It is also interesting to find the inflection point of the free-energy density, Eq. (33), as a function of R for the isotropic phase. For $c = 0$, from Eq. (35a), one obtains the stability condition

$$\frac{\kappa\mu^2}{4} - \frac{\nu\Lambda}{4R^{\frac{3}{2}}} > 0 \Longrightarrow \frac{\Lambda}{\kappa A^{\frac{3}{2}}} < \sqrt{\frac{\mu}{2\nu^2}} = \frac{1}{p_0^*}. \tag{42a}$$

From Eqs. (27) and (30) with $c = 0$, $A = \mu M_0 = \mu R/2$. Then Eq. (35b) with $c = 0$ yields

$$A < A_0. \tag{42b}$$

Hence there are two ways in which the isotropic phase may become unstable: For sufficiently negative line tension, if the area reaches the target area A_0, anisotropic phases emerge from the isotropic phase as shown in Figs. 6 and 7. In turn, if the scaled line tension surpasses $1/p_0^*$, the homogeneous isotropic phase becomes unstable, cf. Fig. 8, but homogeneous anisotropic phases are not stable either. While Fig. 8 seems to suggest that the cells shrink to zero area (collapsed cells [42]), it could also happen that spatially nonhomogeneous phases may appear.

VI. KINETIC COEFFICIENTS AND EQUATION OF MOTION FOR THE SHAPE TENSOR

Now that we know the behavior of the vertex free energy in terms of the variables R and c introduced in the parametrization of the shape tensor, let us come back to the coarse-graining procedure of Sec. III. As discussed above, since in general G_{ij} varies in space, we have to add the term f_{int} of Eq. (15) to the free-energy density that penalizes gradients, where for simplicity we used a one-constant approximation (cf. Frank elasticity in nematic liquid crystals [49,51]). Then, the coarse-grained free-energy density, Eq. (14), is the sum of the single-cell free-energy density, Eq. (33) and the interaction part, Eq. (15). The resulting free-energy density is

$$f_V = \frac{\kappa}{2}\left(\frac{\mu R}{2\cosh c} - A_0\right)^2 + \frac{\Gamma\nu^2 R}{2} + \Lambda\nu\sqrt{R} + \frac{K_G}{4}|\nabla R|^2 + \frac{K_G}{4}[|\nabla(R\tanh c)|^2 + 4(R\tanh c|\nabla\theta|)^2]. \tag{43}$$

To decide the form of the kinetic coefficients Γ_{ijkl} in Eq. (18), we first derive the following formulas:

$$\frac{D}{Dt}G_{ij} = \frac{\delta_{ij}}{2}\frac{dR}{dt} + \frac{\Theta_{ij}}{2}\frac{d}{dt}(R\tanh c) + \frac{R}{2}\tanh c\left(\frac{d\theta}{dt} + \frac{\partial_1 v_2 - \partial_2 v_1}{2}\right)\frac{\partial\Theta_{ij}}{\partial\theta}, \tag{44a}$$

$$D_{ik}G_{kj} + G_{ik}D_{kj} = \frac{R}{2}\tanh c[(\partial_1 v_1 - \partial_2 v_2)\cos 2\theta + (\partial_1 v_2 + \partial_2 v_1)\sin 2\theta]\delta_{ij} + RD_{ij}, \tag{44b}$$

$$\begin{aligned}\frac{D}{Dt}G_{ij} - D_{ik}G_{kj} - G_{ik}D_{kj} = {} & \frac{\delta_{ij} + \Theta_{ij}\tanh c}{2}\left(\frac{dR}{dt} - \big[(\partial_1 v_1 - \partial_2 v_2)\cos 2\theta + (\partial_1 v_2 + \partial_2 v_1)\sin 2\theta\big]R\tanh c\right)\\ & + \frac{R\Theta_{ij}}{2}\left(\frac{1}{\cosh^2 c}\frac{dc}{dt} + \big[(\partial_1 v_1 - \partial_2 v_2)\cos 2\theta + (\partial_1 v_2 + \partial_2 v_1)\sin 2\theta\big]\tanh^2 c\right)\\ & + \frac{R}{2}\tanh c\left(\frac{d\theta}{dt} + \frac{\partial_1 v_2 - \partial_2 v_1}{2}\right)\frac{\partial\Theta_{ij}}{\partial\theta} - RD_{ij} = -\Gamma_{iikl}\frac{\delta\mathcal{F}}{\delta G_{kl}},\end{aligned} \tag{44c}$$

$$\frac{\partial}{\partial G_{kl}}\text{Tr}G = \delta_{kl}, \quad \frac{\partial}{\partial G_{kl}}\text{det}G = (\text{det}G)G_{kl}^{-1} = R\delta_{kl} - G_{kl} = \frac{R}{2}\delta_{kl} - \frac{R\tanh c}{2}\Theta_{kl}, \tag{44d}$$

where (44c) is just an expanded version of (18). Using Eq. (44d), from Eq. (43) we obtain

$$\begin{aligned}\frac{\delta\mathcal{F}}{\delta G_{kl}} = {} & \frac{\delta_{kl}}{2}\left[\kappa\mu\left(\frac{\mu R}{2} - A_0\cosh c\right) + \Gamma\nu^2 + \frac{\Lambda\nu}{\sqrt{R}} - K_G\nabla^2 R\right] - \Theta_{kl}\left[\frac{\kappa\mu}{2}\left(\frac{\mu R}{2\cosh c} - A_0\right)\sinh c\right.\\ & \left. + \frac{K_G}{2}[\nabla^2(R\tanh c) - 4R\tanh c\,|\nabla\theta|^2]\right] - \frac{K_G}{2}[R\tanh c\,\nabla^2\theta + 2\nabla\theta\cdot\nabla(R\tanh c)]\frac{\partial\Theta_{kl}}{\partial\theta}.\end{aligned} \tag{45}$$

Note that the matrices δ_{ij}, Θ_{ij}, and $\partial\Theta_{ij}/\partial\theta$ appearing in Eqs. (44) and (45) are orthogonal with respect to the scalar product $\text{Tr}(A_{ik}B_{kj})$ and form a basis in the corresponding vector space. Thus, the kinetic coefficients can be written as linear combinations of products of these matrices. We will select them by imposing that, at zero average flow velocity, $v = 0$, Eq. (18) should yield a gradient system for homogeneous phases compatible with the thermodynamic stability established in the preceding section.

According to Eq. (44c), the evolution equation for R can be found by taking the trace, thereby obtaining

$$\frac{dR}{dt} = R\tanh c[(\partial_1 v_1 - \partial_2 v_2)\cos 2\theta + (\partial_1 v_2 + \partial_2 v_1)\sin 2\theta] - \Gamma_{iikl}\frac{\delta\mathcal{F}}{\delta G_{kl}}. \tag{46}$$

For Eq. (46) to be a gradient vector field for zero velocity, we consider

$$\frac{\delta\mathcal{F}}{\delta R} = \frac{\delta\mathcal{F}}{\delta G_{kl}}\frac{\partial G_{kl}}{\partial R} = \frac{\delta\mathcal{F}}{\delta G_{kl}}\frac{G_{kl}}{R}.$$

Thus, we should select $\Gamma_{iikl} = \gamma_1 G_{kl}/R = \gamma_1 R(\delta_{kl} + \tanh c\,\Theta_{kl})/2$.

Similarly, $\dot{c}$ in Eq. (44a) has a prefactor $R\Theta_{ij}/(2\cosh^2 c)$ and, therefore, the kinetic coefficient in its equation has to produce the gradient vector field $-\gamma_2 R\Theta_{ij}[\delta\mathcal{F}/\delta c]/(2\cosh^2 c)$, where

$$\frac{\delta\mathcal{F}}{\delta c} = \frac{\delta\mathcal{F}}{\delta G_{kl}}\frac{\partial G_{kl}}{\partial c} = \frac{\delta\mathcal{F}}{\delta G_{kl}}\frac{R\,\Theta_{kl}}{2\cosh^2 c} = \frac{\partial f_{\text{sc}}}{\partial c} - \frac{K_G R}{2\cosh^2 c}[\nabla^2(R\tanh c) - 4R\tanh c|\nabla\theta|^2].$$

The first line suggests a second contribution to the kinetic coefficient. We choose a third one, as explained below, and write

$$\Gamma_{ijkl} = \gamma_1\frac{G_{ij}G_{kl}}{R^2} + \gamma_2\frac{R^2\Theta_{ij}\Theta_{kl}}{4\cosh^4 c} + \frac{\gamma_3}{8}\frac{\partial\Theta_{ij}}{\partial\theta}\frac{\partial\Theta_{kl}}{\partial\theta}. \tag{47}$$

Note that the kinetic coefficients Γ_{ijkl} have to be symmetric with respect to the exchanges $ij \leftrightarrow ji$ and in $kl \leftrightarrow lk$ (because stress and shear are symmetric tensors) and $ij \leftrightarrow kl$ (Onsager relation) [48], which is all fulfilled by our choice.

Looking now at the traceless part of Eq. (18) in the form of Eq. (44c), using (46) and (47), we get

$$A\Theta_{ij} + \frac{B}{2}\frac{\partial\Theta_{ij}}{\partial\theta} = RD_{ij}, \tag{48a}$$

where A and B are the coefficients of Θ_{ij} and of $(\partial\Theta_{ij}/\partial\theta)/2$ in Eqs. (44c) and (18):

$$A = \frac{R}{2\cosh^2 c}\left(\frac{dc}{dt} + \gamma_2\frac{\partial f_{\text{sc}}}{\partial c} + \mathcal{A}\sinh^2 c - \gamma_2 K_G[\nabla^2(R\tanh c) - 4R\tanh c|\nabla\theta|^2]\right), \tag{48b}$$

$$B = R\tanh c\left(\frac{d\theta}{dt} + \frac{\partial_1 v_2 - \partial_2 v_1}{2} - \gamma_3 K_G[\nabla^2\theta + 2\nabla\theta\cdot\nabla\ln(R\tanh c)]\right), \tag{48c}$$

$$\mathcal{A} = (\partial_1 v_1 - \partial_2 v_2)\cos 2\theta + (\partial_1 v_2 + \partial_2 v_1)\sin 2\theta. \tag{48d}$$

Equation (48a) is equivalent to

$$\left(A\cos 2\theta - B\sin 2\theta - R\frac{\partial_1 v_1 - \partial_2 v_2}{2}\right)\begin{pmatrix}1 & 0\\ 0 & -1\end{pmatrix} = -\left(A\sin 2\theta + B\cos 2\theta - R\frac{\partial_1 v_2 + \partial_2 v_1}{2}\right)\begin{pmatrix}0 & 1\\ 1 & 0\end{pmatrix}. \tag{49}$$

The coefficients of the independent matrices in Eq. (49) have to be zero, which allows us to get the equations for $\frac{dc}{dt}$ and $\frac{d\theta}{dt}$ from (48). Together with Eq. (46), the final equations are

$$\frac{dR}{dt} = R\tanh c\,[(\partial_1 v_1 - \partial_2 v_2)\cos 2\theta + (\partial_1 v_2 + \partial_2 v_1)\sin 2\theta] - \gamma_1\frac{\partial f_{\text{sc}}}{\partial R} + \frac{\gamma_1 K_G}{2}[\nabla^2 R + \tanh c\nabla^2(R\tanh c) - 4R\tanh^2 c|\boldsymbol{\nabla}\theta|^2 \tag{50a}$$

$$\frac{dc}{dt} = (\partial_1 v_1 - \partial_2 v_2)\cos 2\theta + (\partial_1 v_2 + \partial_2 v_1)\sin 2\theta - \gamma_2\frac{\partial f_{\text{sc}}}{\partial c} + \frac{\gamma_2 K_G R}{2\cosh^2 c}[\nabla^2(R\tanh c) - 4R\tanh c|\boldsymbol{\nabla}\theta|^2], \tag{50b}$$

$$\frac{d\theta}{dt} = -\frac{\partial_1 v_2 - \partial_2 v_1}{2} + \frac{(\partial_1 v_2 + \partial_2 v_1)\cos 2\theta - (\partial_1 v_1 - \partial_2 v_2)\sin 2\theta}{2\tanh c} + \gamma_3 K_G\,[\nabla^2\theta + 2\boldsymbol{\nabla}[\ln(R\tanh c)]\cdot\boldsymbol{\nabla}\theta]. \tag{50c}$$

In the equation for $\dot{\theta}$, we used that

$$\frac{\delta\mathcal{F}}{\delta G_{kl}}\frac{\partial\Theta_{kl}}{\partial\theta} = -4K_G[R\tanh c\,\nabla^2\theta + 2\nabla(R\tanh c)\cdot\nabla\theta].$$

Hence the choice of the contribution proportional to γ_3 in Eq. (47) leads to Eq. (50c) becoming a diffusion equation for the angle.

Equations (50) conclude the coarse-graining procedure. Our choice of the Onsager coefficients, Eq. (47)—motivated by the fact that the homogeneous steady states of the dynamic equations should be equivalent to the minima of the single cell free energy—allowed us to derive consistent and closed hydrodynamic equations from microscopic dynamics. Moreover, we were able to give a compact form of these equations in only three scalar variables (R, c, and θ) that are easy to interpret.

VII. HOMOGENEOUS PHASES AT ZERO FLOW VELOCITY

For homogeneous phases at zero velocity, R and c depend only on time, and Eq. (50) become (putting all contributions in v and K_G to zero)

$$\dot{R} = -\gamma_1\frac{\partial f_{\text{sc}}}{\partial R} = -\frac{\gamma_1\kappa\mu}{2\cosh c}\left(\frac{\mu R}{2\cosh c} - A_0\right) - \frac{\gamma_1}{2}\left(\frac{\Lambda\nu}{\sqrt{R}} + \Gamma\nu^2\right), \tag{51a}$$

$$\dot c = -\gamma_2 \frac{\partial f_{\rm sc}}{\partial c} = \gamma_2 \frac{R\kappa\mu \tanh c}{2\cosh c}\left(\frac{\mu R}{2\cosh c} - A_0\right), \tag{51b}$$

$$\dot\theta = 0. \tag{51c}$$

The stationary solutions of Eq. (51) are—by construction, i.e., by the choice of the dissipative coefficients—exactly the homogeneous phases already discussed in Sec. V. Their linear stability depends on the eigenvalues of the Jacobian matrix

$$J = \begin{pmatrix} -\gamma_1 \frac{\partial^2 f_{\rm sc}}{\partial R^2} & -\gamma_1 \frac{\partial^2 f_{\rm sc}}{\partial R \partial c} \\ -\gamma_2 \frac{\partial^2 f_{\rm sc}}{\partial R \partial c} & -\gamma_2 \frac{\partial^2 f_{\rm sc}}{\partial c^2} \end{pmatrix}. \tag{52}$$

The stability criteria in Eq. (35) (corresponding to a positive definite Hessian matrix of the single cell free energy density $f_{\rm sc}$) ensure that the eigenvalues of the Jacobian (52) are negative and, therefore, that the homogeneous phases are dynamically stable. This is further illustrated by the phase space portraits [52] of the dynamical system defined by Eqs. (51a) and (51b). If $\Lambda > \Lambda^* = -\Gamma\nu\sqrt{2A_0/\mu}$, the only stationary solution is isotropic and a stable node as shown in Fig. 9. For $\Lambda < \Lambda^*$, the isotropic solution becomes an unstable saddle point and there are two symmetric anisotropic solutions that are stable nodes, as illustrated in Fig. 10. The anisotropic phases emerge from the homogeneous phase at $\Lambda = \Lambda^*$, cf. the pitchfork bifurcation shown in Fig. 7.

The area $A = \mu R/(2\cosh c)$ calculated from homogeneous phases, i.e., stationary solutions of Eq. (51), increases with negative line tension, from $\Lambda = 0$ to $-\Lambda = |\Lambda^*|$. Then $A = A_0$ in the anisotropic phase for all $\Lambda \leqslant \Lambda^*$.

VIII. HOMOGENEOUS PHASES UNDER SHEAR FLOW

Let us now consider the system under a stationary homogeneous shear flow,

$$v_y = 0, \quad v_x = \dot\gamma y, \tag{53}$$

that solves the continuity equation (16), and, to leading order, the velocity equation (17) (i.e., including σ^D and σ^E, but neglecting a possible feedback of the ordering on the flow as described by σ^G).

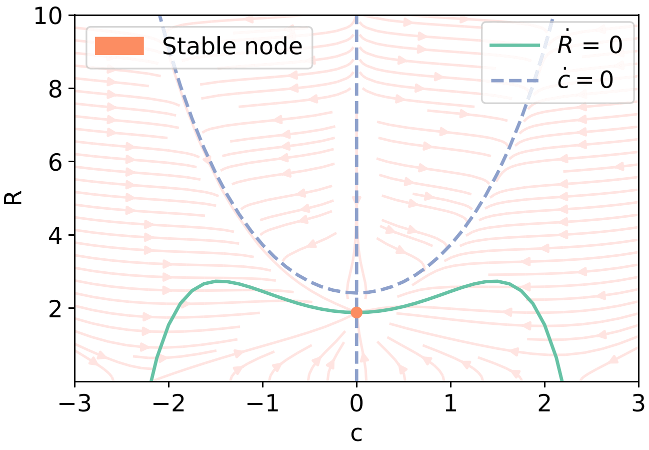

FIG. 9. Phase space portrait of Eq. (51) for $\Lambda = 0$. The only stationary solution occurs at $c = 0$ (isotropic phase) at finite R (thick dot). Shown are the nullclines (thick solid and dashed curves) and the streamlines of the dynamical system (lines with arrows). Here $\kappa = 1$, $n = 6$, $\Gamma = 0.1$, and $A_0 = \pi$.

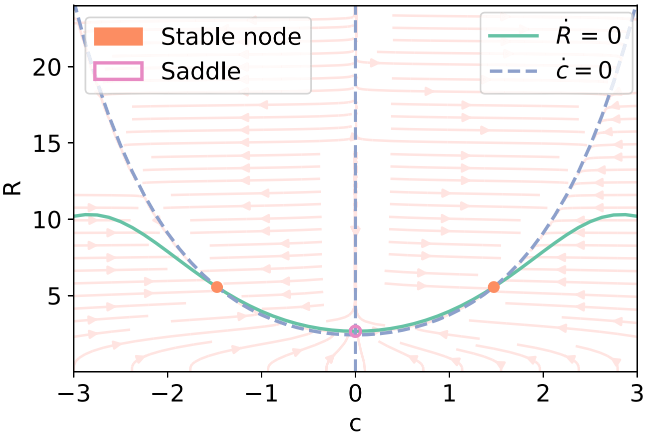

FIG. 10. Same as Fig. 9 for $\Lambda = -1 < \Lambda^*$. There are two $\pm c$-symmetric stable nodes (thick dots) corresponding to the anisotropic phases. The isotropic phase at $c = 0$ (purple dot) becomes a saddle point.

Substituting Eq. (53) into Eq. (50), they become

$$\dot R = \dot\gamma R \tanh c \sin 2\theta - \gamma_1 \frac{\partial f_{\rm sc}}{\partial R}, \tag{54a}$$

$$\dot c = \dot\gamma \sin 2\theta - \gamma_2 \frac{\partial f_{\rm sc}}{\partial c}, \tag{54b}$$

$$\dot\theta = \frac{\dot\gamma}{2}\left(1 + \frac{\cos 2\theta}{\tanh c}\right). \tag{54c}$$

Note that uniform shear introduces a relation between the “director orientation” at angle θ and the cellular anisotropy and perimeter fields, c and R, although the average free energy does not depend on θ.

A. Stationary solutions

The stationary solutions of Eq. (54) satisfy the following system of equations:

$$\dot\gamma R \tanh c \sin 2\theta = \frac{\gamma_1}{2}\left[\frac{\kappa\mu}{\cosh c}\left(\frac{\mu R}{2\cosh c} - A_0\right) + \frac{\Lambda\nu}{\sqrt{R}} + \Gamma\nu^2\right], \tag{55a}$$

$$\dot\gamma \sin 2\theta = -\gamma_2 \frac{\kappa\mu R \sinh c}{2\cosh^2 c}\left(\frac{\mu R}{2\cosh c} - A_0\right), \tag{55b}$$

$$\cos 2\theta = -\tanh c. \tag{55c}$$

Equation (55c) has a solution with $c \leqslant 0$ defined on $-\frac{\pi}{4} < \theta \leqslant \frac{\pi}{4}$, and another with $c > 0$ on $\frac{\pi}{4} < \theta < \frac{3\pi}{4}$. Then, we can write $\sin 2\theta = {\rm sech} c$, which transforms Eqs. (55a) and (55b) into

$$\dot\gamma R \tanh c = \frac{\gamma_1}{2}\left[\kappa\mu\left(\frac{\mu R}{2\cosh c} - A_0\right) + \left(\frac{\Lambda\nu}{\sqrt{R}} + \Gamma\nu^2\right)\cosh c\right], \tag{56a}$$

$$\dot\gamma = -\frac{\gamma_2\kappa\mu R \tanh c}{2}\left(\frac{\mu R}{2\cosh c} - A_0\right). \tag{56b}$$

B. Imperfect pitchfork bifurcation

Let us find out how shear modifies the pitchfork bifurcation of Fig. 7. For small shear, we expect an imperfect bifurcation (cf., e.g., Ref. [53]). For $\dot{\gamma} = 0$, Eq. (56b) has the solutions $c = 0$ and $\cosh c = \mu R/(2A_0)$. Inserting the latter expression into Eq. (56a), we obtain the outer bifurcation diagram on the (c, Λ) plane given by

$$\Lambda = -\Gamma\nu\sqrt{R} = -\Gamma\nu\sqrt{\frac{2A_0}{\mu}\cosh c} \quad \text{and} \quad c = 0. \tag{57}$$

Expanding this expression around $c = 0$, we obtain to leading order

$$R = \frac{2A_0}{\mu}\cosh c \Longrightarrow R = \frac{2A_0}{\mu}\left(1 + \frac{c^2}{2}\right), \tag{58a}$$

$$\Lambda = -\Gamma\nu\sqrt{\frac{2A_0}{\mu}}\left(1 + \frac{c^2}{4}\right) \Longrightarrow \frac{\Lambda - \Lambda^*}{\Lambda^*} = \frac{c^2}{4}. \tag{58b}$$

Thus, the inner limit of the outer pitchfork bifurcation diagram is

$$\left(\frac{\Lambda - \Lambda^*}{-\Lambda^*} + \frac{c^2}{4}\right)c = 0. \tag{59}$$

See Ref. [54] for some background on matched asymptotic expansions. Note that all terms in Eq. (59) are $O(c^3)$.

To obtain the bifurcation diagram modified by a small $\dot{\gamma}$, we first substitute Eq. (56b) into (56a), thereby obtaining

$$\left(\frac{\Lambda\nu}{\sqrt{R}} + \Gamma\nu^2\right)\sinh c = 2\dot{\gamma}\left(\frac{1}{\gamma_2 R} + \frac{R\tanh^2 c}{\gamma_1}\right). \tag{60}$$

Let us now consider how a small shear modifies the immediate neighborhood of the bifurcation point in Fig. 7,

$$R = R^* + r, \quad \Lambda = \Lambda^* + \lambda, \quad c = c, \tag{61}$$

where $R^* = 2A_0/\mu$, and r, c, and λ are small. Equation (59) indicates that $\lambda = O(c^2)$, and Eq. (60) indicates that $\dot{\gamma} = O(c^3)$. Inserting Eq. (61) into (60) and keeping only leading-order terms, we obtain

$$r = -\frac{2\sqrt{R^*}}{\Gamma\nu}\lambda. \tag{62}$$

We now substitute this expression into Eq. (56b) and keep only leading-order terms. The result is

$$\left(\frac{\Lambda - \Lambda^*}{\Gamma\nu\sqrt{R^*}} + \frac{c^2}{4}\right)c = \dot{\gamma}_0, \tag{63a}$$

$$\dot{\gamma}_0 = \frac{\dot{\gamma}}{2\gamma_2\kappa A_0^2}. \tag{63b}$$

Hence the right-hand side of Eq. (63a), given by $\dot{\gamma}_0$, acts as a small imperfection on the pitchfork bifurcation diagram, as shown in Fig. 11. There we have depicted the imperfect bifurcation for both $\dot{\gamma} > 0$ and its mirror image for $\dot{\gamma} < 0$.

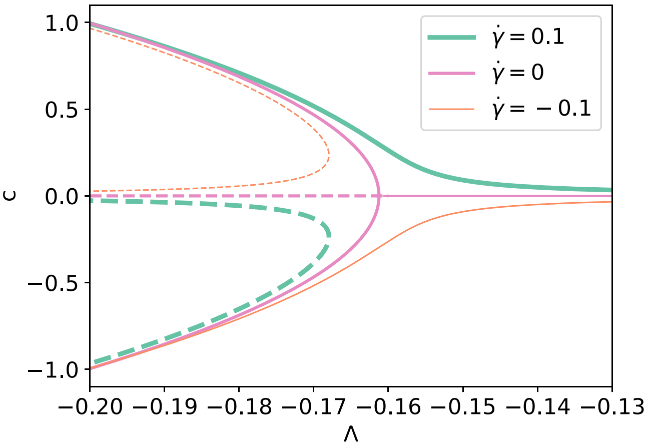

FIG. 11. Imperfect pitchfork bifurcation of Eq. (63a) appearing in the presence of a shear flow on top of the pitchfork bifurcation from Fig. 7, represented by pink curves. Thick (green)/thin (orange) curves correspond to positive/negative shear flow, respectively. Continuous (stable) and dashed (unstable) curves follow from linear stability with eigenvalues given by Eqs. (70) and (71) below. We have also plotted the zero-shear pitchfork bifurcation of Fig. 7. Parameter values are $\kappa = \nu = \gamma_1 = \gamma_2 = 1$, $A_0 = \pi$, $\Gamma = 0.1$, $\mu = 2.4166$, and $\dot{\gamma} = \pm 0.1$.

For positive $\lambda \gg 1$, $c \ll 1$, and Eq. (63a) becomes the hyperbola

$$\lambda\, c = \dot{\gamma}_0 \Gamma\nu\sqrt{R^*}, \tag{64}$$

which is on the half-plane having $\operatorname{sgn} c = \operatorname{sgn}\dot{\gamma}$. The other half-plane contains a turning point having $d\lambda/dc = 0$; see Fig. 11. Together with Eq. (63), this gives the turning point (λ_0, c_0) with

$$c_0 = (-2\dot{\gamma}_0)^{\frac{1}{3}}, \quad r_0 = -\frac{2\sqrt{R^*}\lambda_0}{\Gamma\nu}, \tag{65a}$$

$$\lambda_0 = -3\Gamma\nu\sqrt{R^*}\left(\frac{\dot{\gamma}_0}{4}\right)^{2/3}. \tag{65b}$$

For large values of $|c|$, Eq. (56b) yields Eq. (58a), $R = 2A_0\cosh c/\mu$. Substituting this into Eq. (60) and approximating $\tanh c = \pm 1$ for large c, we find

$$\Lambda = -\sqrt{\frac{2A_0}{\mu}}\left(\Gamma\nu \mp \frac{4\dot{\gamma}A_0}{\gamma_1\mu\nu}\right)\sqrt{\cosh c}. \tag{66a}$$

For consistency with the imperfect bifurcation diagram, we should have

$$\frac{4\dot{\gamma}A_0}{\gamma_1\mu\Gamma\nu^2} < 1. \tag{66b}$$

Equation (63) approximates Eq. (60) and matches the outer solution for $\dot{\gamma}$ given by Eq. (57). In fact, the inner approximation of Eq. (57) is Eq. (59), which clearly matches Eq. (63) as $\dot{\gamma} \to 0$. To find a uniformly valid bifurcation diagram at leading order, we add inner and outer solutions and subtract their common part. After multiplication by $\sqrt{R^*}$, the result is

$$\left(\frac{\Lambda}{\Gamma\nu\sqrt{R^*}} + \sqrt{\cosh c}\right)c = \dot{\gamma}_0, \tag{67}$$

where $\dot{\gamma}_0$ is given by Eq. (63b).

C. Linear stability

To find out the linear stability of the stationary solutions—this time also accounting for spatial degrees of freedom—we linearize Eq. (50) around the stationary solutions obtained from the bifurcation equation (63a) with two simplifying assumptions: (i) we consider periodic boundary conditions on a rectangular box, and (ii) we assume $R - R^* = O(c^2)$, $\Lambda - \Lambda^* = O(c^2)$, $\dot{\gamma} = O(c^3)$. The linearized equations contain terms that depend on y due to the material derivatives. We can eliminate them by shifting $x \to x - \dot{\gamma} y t$. Then, if the unknowns in the linearized equations are proportional to $\exp[\sigma t + ik_1(x - \dot{\gamma} y t) + ik_2 y]$, σ are the eigenvalues of the matrix A_{ij}, where

$$A_{11} = \frac{\dot{\gamma} \sinh c}{\cosh^2 c} - \gamma_1 \left(\frac{\partial^2 f_{\rm sc}}{\partial R^2} + \frac{K_G k^2}{2} (1 + \tanh^2 c) \right), \tag{68a}$$

$$A_{12} = \frac{\dot{\gamma} R}{\cosh^3 c} - \gamma_1 \left(\frac{\partial^2 f_{\rm sc}}{\partial R \partial c} + \frac{K_G k^2 R \sinh c}{2 \cosh^3 c} \right), \tag{68b}$$

$$A_{21} = -\gamma_2 \left(\frac{\partial^2 f_{\rm sc}}{\partial R \partial c} + \frac{K_G k^2 R \sinh c}{2 \cosh^3 c} \right), \tag{68c}$$

$$A_{22} = -\gamma_2 \left(\frac{\partial^2 f_{\rm sc}}{\partial c^2} + \frac{K_G R^2 k^2}{2 \cosh^4 c} \right), \tag{68d}$$

$$A_{13} = -2\dot{\gamma} R \tanh^2 c, \; A_{23} = -2\dot{\gamma} \tanh c, \tag{68e}$$

$$A_{31} = 0, \; A_{32} = \frac{\dot{\gamma}}{\sinh(2c)}, \; A_{33} = -\frac{\dot{\gamma}}{\sinh c} - \gamma_3 K_G k^2, \tag{68f}$$

and $k = \sqrt{k_1^2 + k_2^2}$. Here $f_{\rm sc}$ is given by Eq. (33), and R, c, and θ are the stationary solutions given by Eqs. (61)–(63). Expanding around the bifurcation point R^*, $c^* = 0$, Λ^* with the scaling (ii), we obtain an approximation including up to $O(c^2)$ terms,

$$A_{11} = -\gamma_1 \left(\frac{\partial^2 f_{\rm sc}}{\partial R^2} + \frac{K_G k^2}{2} (1 + c^2) \right), \tag{69a}$$

$$A_{12} = -\gamma_1 \left(\frac{\partial^2 f_{\rm sc}}{\partial R \partial c} + \frac{K_G k^2 R^* c}{2} \right), \tag{69b}$$

$$A_{21} = -\gamma_2 \left(\frac{\partial^2 f_{\rm sc}}{\partial R \partial c} + \frac{K_G k^2 R^* c}{2} \right), \tag{69c}$$

$$A_{22} = -\gamma_2 \left(\frac{\partial^2 f_{\rm sc}}{\partial c^2} + \frac{K_G R^* k^2}{2} (R^* + r - 2R^* c^2) \right), \tag{69d}$$

$$A_{13} = A_{23} = A_{31} = 0, \tag{69e}$$

$$A_{32} = \frac{\dot{\gamma}}{2c}, \quad A_{33} = -\frac{\dot{\gamma}}{c} - \gamma_3 K_G k^2, \tag{69f}$$

$$\frac{\partial^2 f_{\rm sc}}{\partial R^2} = \frac{\kappa \mu^2 (1 - c^2) + \Gamma \nu^2}{4} - \frac{3 \Gamma \nu^2 r}{8 R^{*2}} - \frac{\lambda \nu}{4 R^{*3/2}}, \tag{69g}$$

$$\frac{\partial^2 f_{\rm sc}}{\partial c^2} = \frac{3 \kappa A_0^2 c^2}{2}, \quad \frac{\partial^2 f_{\rm sc}}{\partial R \partial c} = -\kappa \mu A_0 c. \tag{69h}$$

Expanding by minors, Eqs. (69e) and (69f) imply that the determinant $\det(A - \sigma I)$ is $(A_{33} - \sigma)$ times $\det(A_{ij} - \sigma \delta_{ij})$ $(i, j = 1, 2)$. Thus, one eigenvalue is

$$\sigma_3 = -\frac{\dot{\gamma}}{c} - \gamma_3 K_G k^2. \tag{70}$$

Equation (70) states that the stationary solutions with $\dot{\gamma} c > 0$ (corresponding to continuous branches existing for all values of Λ in Fig. 11) are always stable. In contrast, the branches issuing from the turning points in Fig. 11 are unstable for wave numbers on the interval $0 < k^2 < -\dot{\gamma}/(\gamma_3 K_G c)$. They will produce spatially nonhomogeneous solutions when the size of the tissue exceeds a critical value. Here the kinetic coefficient γ_3 plays a stabilizing role.

The other two eigenvalues are those of the submatrix given by Eqs. (69a)–(69d). We find

$$\sigma_1 = -\frac{\gamma_1}{4} \left(\kappa \mu^2 + \frac{\Gamma \nu^2}{R^*} + 2 K_G k^2 \right) + O(c^2), \tag{71a}$$

$$\begin{aligned} \sigma_2 = -\frac{\gamma_2}{2} \Bigg[& K_G R^* k^2 (R^* + 2r + 2c^2) + \kappa A_0 (3 A_0 c^2 - \mu r) \\ & + \frac{8 \gamma_1 A_0^2 c^2 (\kappa \mu - K_G k^2/\mu)^2}{\gamma_1 (\kappa \mu^2 + \frac{\Gamma \nu^2}{R^*} + 2 K_G k^2) - 2 \gamma_2 K_G R^{*2} k^2} \Bigg] + O(c^3), \end{aligned} \tag{71b}$$

provided the denominator in the last term of Eq. (71b) is $O(1)$. If this denominator vanishes for some value of the parameters, the eigenvalues become

$$\begin{aligned} \sigma_{1,2} = & -\frac{\gamma_1}{4} \left(K_G k^2 + \frac{\kappa \mu^2}{2} + \frac{\Gamma \nu^2}{2R^*} \right) - \frac{2\gamma_2}{\mu^2} A_0^2 K_G k^2 \\ & \pm \sqrt{\gamma_1 \gamma_2} A_0 |c| \left| \frac{K_G k^2}{\mu} - \frac{\kappa \mu}{2} \right| + O(c^2). \end{aligned} \tag{72}$$

In all cases, these eigenvalues are negative and the stability of the homogeneous phases under shear is decided by Eq. (70) alone.

IX. CONCLUSIONS

In this work, we have derived macroscopic hydrodynamic equations to describe a monolayer of confluent cells. We started from the mesoscopic vertex model, which provides a convenient average single-cell free-energy density in terms of the cell area and perimeter. These quantities can be related to an average shape tensor, which can be written in terms of three fields: R (trace, proportional to perimeter square), c (anisotropy), and θ (angle of the director field describing the nematiclike alignment of elongated cells). Hydrodynamic equations follow from a coarse-graining procedure using Poisson brackets [25]. The reactive part of the hydrodynamic equations is a straightforward consequence of averaging the Poisson brackets of microscopic quantities, i.e., density, momentum and shape tensor. The dissipative part of the equations depends on the choice of the kinetic coefficients and the average free energy. Our consistent choice produces a gradient system for homogeneous phases, which have the same dynamic stability properties as the thermodynamic stability of their homogeneous counterpart.

Thus, we could recover the solid-liquid transition for a critical value of the line tension, which appears as a supercritical pitchfork bifurcation between isotropic cells ($c = 0$) and elongated cells with nonzero anisotropy field c. Furthermore, we have analyzed how a homogeneous shear flow converts this transition into an imperfect pitchfork bifurcation. There, the continuous branches are stable, even including spatial degrees of freedom, while the saddle-node branches are unstable versus spatially inhomogeneous states in sufficiently large monolayers. These predictions should be accessible to dedicated simulations of the vertex model under shear, similar to [37], which investigated nonlinear response to shear, but with a parallel analysis of the coarse-grained dynamics of the shape tensor.

It should be noted that, although the solid-liquid transition is present in the model, the dynamic equations are hydrodynamical in nature. To describe the solid dynamics faithfully, complementary approaches have to be developed. One route could be based on Ref. [38]. There, the metric tensor is introduced in addition to the shape tensor (called the network tensor there). This allows to describe elastic effects. Another approach could start from recently developed microscopic theories of sheared jammed soft particles [55]. Potentially this could capture the yield stress behavior recently demonstrated in the vertex model [56] when shearing the elastic phase.

In the future, the coarse-grained equations for a tissue obtained here can be investigated for several biologically relevant situations—for instance, having spatially varying parameters in the equations. An interesting related question is the stability of a boundary between two tissues that have different line tensions, as in antagonistic migration assays of two cell populations [16,17]. Conceptually, the most important next step would be to incorporate activity into the coarse-graining process. Active, e.g., contractile, elements have been included in phenomenological and mechanical approaches to tissues [22,23], and active dynamics similar to Eqs. (3) and (4) have been coarse-grained to yield Vicsek-type models [57,58]. However, a systematic coarse-graining of these effects on the tissue level has not yet been undertaken.

ACKNOWLEDGMENTS

This work has been supported by the FEDER/Ministerio de Ciencia, Innovación y Universidades–Agencia Estatal de Investigación Grant No. PID2020-112796RB-C22, by the Madrid Government (Comunidad de Madrid-Spain) under the Multiannual Agreement with UC3M in the line of Excellence of University Professors (EPUC3M23), and in the context of the V PRICIT (Regional Programme of Research and Technological Innovation). F.Z. was supported by the Deutsche Forschungsgemeinschaft (DFG, German Research Foundation) under Germanys Excellence Strategy EXC 2181/1 - 390900948 (the Heidelberg STRUCTURES Excellence Cluster).

---

[1] S. F. Gilbert and M. J. F. Barresi, *Developmental Biology*, 11th ed. (Sinauer Associates, Sunderland, MA, 2018).
[2] V. Hakim and P. Silberzan, Collective cell migration: A physics perspective, Rep. Prog. Phys. **80**, 076601 (2017).
[3] X. Trepat and E. Sahai, Mesoscale physical principles of collective cell organization, Nat. Phys. **14**, 671 (2018).
[4] F. Giavazzi, M. Paoluzzi, M. Macchi, D. Bi, G. Scita, L. Manning, R. Cerbino, and C. Marchetti, Flocking transition in confluent tissues, Soft Matter **14**, 3471 (2018).
[5] R. Alert and X. Trepat, Physical models of collective cell migration, Annu. Rev. Condens. Matter Phys. **11**, 77 (2020).
[6] J. Löber, F. Ziebert, and I. S. Aranson, Collisions of deformable cells lead to collective migration, Sci. Rep. **5**, 9172 (2015).
[7] R. Mayor and S. Etienne-Manneville, The front and rear of collective cell migration, Nat. Rev. Mol. Cell Biol. **17**, 97 (2016).
[8] B. Stramer and R. Mayor, Mechanisms and *in vivo* functions of contact inhibition of locomotion, Nat. Rev. Mol. Cell Biol. **18**, 43 (2017).
[9] B. Ladoux and R.-M. Mège, Mechanobiology of collective cell behaviours, Nat. Rev. Mol. Cell Biol. **18**, 743 (2017).
[10] W. Xi, T. B. Saw, D. Delacour, C. T. Lim, and B. Ladoux, Material approaches to active tissue mechanics, Nat. Rev. Mater. **4**, 23 (2019).
[11] M. Poujade, E. Grasland-Mongrain, A. Hertzog, J. Jouanneau, P. Chavrier, B. Ladoux, A. Buguin, and P. Silberzan, Collective migration of an epithelial monolayer in response to a model wound, Proc. Natl. Acad. Sci. USA **104**, 15988 (2007).
[12] M. Abercrombie and E. J. Ambrose, Surface properties of cancer cells: A review, Cancer Res. **22**, 525 (1962).
[13] P. Friedl and D. Gilmour, Collective cell migration in morphogenesis, regeneration and cancer, Nature Rev. Mol. Cell Biol. **10**, 445 (2009).
[14] E. Ben-Jacob, D. S. Coffey, and H. Levine, Bacterial survival strategies suggest rethinking cancer cooperativity, Trends Microbiol. **20**, 403 (2012).
[15] K.-J. Streitberger, L. Lilaj, F. Schrank, J. Braun, K. T. Hoffmann, M. Reiss-Zimmermann, J. A. Käs, and I. Sack, How tissue fluidity influences brain tumor progression, Proc. Natl. Acad. Sci. USA **117**, 128 (2020).
[16] S. Moitrier, C. Blanch-Mercader, S. Garcia, K. Sliogeryte, T. Martin, J. Camonis, P. Marcq, P. Silberzan, and I. Bonnet, Collective stresses drive competition between monolayers of normal and Ras-transformed cells, Soft Matter **15**, 537 (2019).
[17] L. L. Bonilla, A. Carpio, and C. Trenado, Tracking collective cell motion by topological data analysis, PLoS Comput. Biol. **16**, e1008407 (2020).
[18] L. Hufnagel, A. A. Teleman, H. Rouault, S. M. Cohen, and B. I. Shraiman, On the mechanism of wing size determination in fly development, Proc. Natl. Acad. Sci. USA **104**, 3835 (2007).
[19] T. Lecuit, P. F. Lenne, and E. Munro, Force generation, transmission, and integration during cell and tissue morphogenesis, Annu. Rev. Cell Dev. Biol. **27**, 157 (2011).
[20] K. Goodwin and C. M. Nelson, Mechanics of development, Devel. Cell **56**, 240 (2021).
[21] M. C. Marchetti, J. F. Joanny, S. Ramaswamy, T. B. Liverpool, J. Prost, M. Rao, and R. A. Simha, Hydrodynamics of soft active matter, Rev. Mod. Phys. **85**, 1143 (2013).
[22] S. Tlili, C. Gay, F. Graner, P. Marcq, F. Molino, and P. Saramito, Colloquium: Mechanical formalisms for tissue dynamics, Eur. Phys. J. E **38**, 33 (2015).
[23] S. Ishihara, P. Marcq, and K. Sugimura, From cells to tissue: A continuum model of epithelial mechanics, Phys. Rev. E **96**, 022418 (2017).

[24] M. Merkel, R. Etournay, M. Popović, G. Salbreux, S. Eaton, and F. Jülicher, Triangles bridge the scales: Quantifying cellular contributions to tissue deformation, Phys. Rev. E **95**, 032401 (2017).

[25] A. Hernandez and M. C. Marchetti, Poisson-bracket formulation of dynamics of fluids of deformable particles, Phys. Rev. E **103**, 032612 (2021).

[26] A, G. Fletcher, M. Osterfield, R. E. Baker, and S. Y. Shvartsman, Vertex models of epithelial morphogenesis, Biophys. J. **106**, 2291 (2014).

[27] S. Alt, P. Ganguly, and G. Salbreux, Vertex models: From cell mechanics to tissue morphogenesis, Philos. Trans. R. Soc. B **372**, 20150520 (2017).

[28] H. Honda, M. Tanemura, and T. Nagai, A three-dimensional vertex dynamics cell model of space-filling polyhedra simulating cell behavior in a cell aggregate, J. Theor. Biol. **226**, 439 (2004).

[29] R. Farhadifar, J.-C. Röper, B. Aigouy, S. Eaton, and F. Jülicher, The influence of cell mechanics, cell-cell interactions, and proliferation on epithelial packing, Curr. Biol. **17**, 2095 (2007).

[30] F. Graner, Y. Jiang, E. Janiaud, and C. Flament, Equilibrium states and ground state of two-dimensional fluid foams, Phys. Rev. E **63**, 011402 (2000).

[31] D. Weaire and N. Rivier, Soap, cells and statistics–random patterns in two dimensions, Contemp. Phys. **25**, 59 (1984).

[32] D. Bi, J. H. Lopez, J. M. Schwarz, and M. L. Manning, Energy barriers and cell migration in densely packed tissues, Soft Matter **10**, 1885 (2014).

[33] D. Bi, J. H. Lopez, J. M. Schwarz, and M. L. Manning, A density-independent rigidity transition in biological tissues, Nat. Phys. **11**, 1074 (2015).

[34] C. Malinverno, S. Corallino, F. Giavazzi, M. Bergert, Q. Li, M. Leoni, A. Disanza, E. Frittoli, A. Oldani, E. Martini, T. Lendenmann, G. Deflorian, G. V. Beznoussenko, D. Poulikakos, K. H. Ong, M. Uroz, X. Trepat, D. Parazzoli, P. Maiuri, W. Yu, A. Ferrari, R. Cerbino, and G. Scita, Endocytic reawakening of motility in jammed epithelia, Nat. Mater. **16**, 587 (2017).

[35] G. Mazenko, *Nonequilibrium Statistical Mechanics* (Wiley-VCH, Weinheim, 2006).

[36] P. Chaikin and T. Lubensky, *Principles of Condensed Matter Physics* (Cambridge University Press, Cambridge, 1995).

[37] M. J. Hertaeg, S. M. Fielding, and D. Bi, Discontinuous shear thickening in biological tissue rheology, arXiv:2211.15015.

[38] D. Grossman and J.-F. Joanny, Instabilities and geometry of growing tissues, Phys. Rev. Lett. **129**, 048102 (2022).

[39] D. Barton, S. Henkes, C. Weijer, and R. Sknepnek, Active Vertex Model for cell-resolution description of epithelial tissue mechanics, PLoS Comput. Biol. **13**, e1005569 (2017).

[40] J.-Q. Lv, P.-C. Chen, W. T. Góźdź, and B. Li, Mechanical adaptions of collective cells nearby free tissue boundaries, J. Biomech. **104**, 109763 (2020).

[41] L. Valencia, V. López-Llorente, J. C. Lasheras, J. L. Jorcano, and J. Rodríguez-Rodríguez, Interaction of a migrating cell monolayer with a flexible fiber, Biophys. J. **120**, 539 (2021).

[42] D. B. Staple, R. Farhadifar, J.-C. Röper, B. Aigouy, S. Eaton, and F. Jülicher, Mechanics and remodelling of cell packings in epithelia, Eur. Phys. J. E **33**, 117 (2010).

[43] T. Hiraiwa, E. Kuranaga, and T. Shibata, Wave propagation of junctional remodeling in collective cell movement of epithelial tissue: Numerical simulation study, Front. Cell Dev. Biol. **5**, 66 (2017).

[44] Soft Active Matter on Surfaces (SAMoS), https://github.com/sknepneklab/SAMoS.

[45] M. Czajkowski, D. Bi, L. M. Manning, and M. C. Marchetti, Hydrodynamics of shape-driven rigidity transitions in motile tissues, Soft Matter **14**, 5628 (2018).

[46] R. Zwanzig, *Nonequilibrium Statistical Mechanics* (Oxford University Press, Oxford, UK, 2000).

[47] H. Stark and T. C. Lubensky, Poisson-bracket approach to the dynamics of nematic liquid crystals, Phys. Rev. E **67**, 061709 (2003).

[48] S. R. De Groot and P. Mazur, *Non-Equilibrium Thermodynamics* (Dover, NY, 1984).

[49] P. G. De Gennes and J. Prost, *The Physics of Liquid Crystals* (Oxford University Press, Oxford, UK, 1993).

[50] T. B. Saw, W. Xi, B. Ladoux, and C. T. Lim, Biological tissues as active nematic liquid crystals, Adv. Mater. **30**, 1802579 (2018).

[51] L. D. Landau and E. M. Lifshitz, *Theory of Elasticity*, 3rd ed. (Pergamon, New York, 1986).

[52] S. H. Strogatz, *Nonlinear Dynamics and Chaos* (Perseus Books, Cambridge, MA, 1994).

[53] G. Iooss and D. D. Joseph, *Elementary Stability and Bifurcation Theory*, 2nd ed. (Springer New York, 1990).

[54] C. M. Bender and S. A. Orszag, *Advanced Mathematical Methods for Scientists and Engineers* (McGraw-Hill, New York, 1978).

[55] N. Cuny, R. Mari, and E. Bertin, Microscopic theory for the rheology of jammed soft suspensions, Phys. Rev. Lett. **127**, 218003 (2021).

[56] M. Popović, V. Druelle, N. A. Dye, F. Jülicher, and M. Wyart, Inferring the flow properties of epithelial tissues from their geometry, New J. Phys. **23**, 033004 (2021).

[57] E. Bertin, M. Droz, and G. Grégoire, Boltzmann and hydrodynamic description for self-propelled particles, Phys. Rev. E **74**, 022101 (2006).

[58] F. D. C. Farrell, M. C. Marchetti, D. Marenduzzo, and J. Tailleur, Pattern formation in self-propelled particles with density-dependent motility, Phys. Rev. Lett. **108**, 248101 (2012).